

Implicit Large Eddy Simulation of Transitional Flow over a SD7003 Wing Using High-order Spectral Difference Method

Ying Zhou¹ and Z.J. Wang²

Department of Aerospace Engineering and CFD Center, Iowa State University, Ames, IA 50011

The transitional flow with a laminar separation bubble over a SD7003 wing at a low Reynolds number $Re = 6 \times 10^4$ and angle of attack $AoA = 4.0 \text{ deg}$ is numerically computed using implicit large eddy simulation with a spectral difference method on unstructured hexahedral meshes. The averaged and statistical results are compared with previously published results. A laminar separation bubble forms after the flow detaches from the suction side of the wing. After the vortex breakdown, the separated flow transitions to turbulent flow and reattaches to the wall. The origin and growth of the initial disturbances are investigated. The vortex breakdown process and the transition mechanism are described and discussed.

I. Introduction

Low Reynolds number flow has been of interest for decades because of the development of Micro Air Vehicles (MAV). A numerical investigation of the flow over the SD7003 wing at angle of attack $AoA = 4.0 \text{ deg}$, and Reynolds number $Re = 6 \times 10^4$ is presented in this paper. The SD7003 wing and flow conditions are chosen due to the availability of high-resolution numerical and experimental data^{15,20,24,25}.

High-order methods on unstructured grids are known for their advantages of accuracy and flexibility in the numerical simulation of multi-scale flow with complex geometries. In the last two decades, there have been intensive research efforts on high-order methods for unstructured grids¹⁻¹³. In this paper, a high-order SD method for the three dimensional Navier-Stokes equations on unstructured hexahedral grids developed by Sun et al.¹³ is used. Both the attached/detached laminar flow and the reattached turbulent flow exist on the suction side of the wing at the current flow condition. The Implicit Large Eddy Simulation (ILES) approach is employed to capture the laminar separation and the vortex breakdown.

Since laminar boundary layers are less resistible to the significant adverse pressure gradient, laminar separation bubbles (LSB) are widely found over the suction side of low-Reynolds-number airfoils at moderate incidences. The behavior of the LSB is known to significantly affect the aerodynamic performance of the airfoils. After separation, the separated laminar boundary layers rapidly transition to turbulence. Attached turbulent boundary layers form after the vortex breakdown. But the details of the breakdown process are not clearly understood yet. A good physical understanding of the formation of the LSB and the mechanism of the vortex breakdown would help improve the aerodynamic performance of MAVs.

The rest of the paper is organized as follows. In the next section, the numerical method is briefly reviewed. In section III, averaged and statistical results are presented, and comparisons with the results from previously published data are made. In section IV, the transition process including the origin and growth of the initial disturbances, the breakdown mechanism and the formation of the turbulent vortex packet are extensively investigated and discussed. Concluding remarks are given in section V.

II. Review of Multidomain Spectral Difference (SD) Method

Governing equations

Consider the three-dimensional compressible non-linear Navier-Stokes equations written in the conservation form as

$$\frac{\partial Q}{\partial t} + \frac{\partial F}{\partial x} + \frac{\partial G}{\partial y} + \frac{\partial H}{\partial z} = 0 \quad (2.1a)$$

on domain $\Omega \times [0, T]$ and $\Omega \subset R^3$ with the initial condition

$$Q(x, y, z, 0) = Q_0(x, y, z) \quad (2.1b)$$

¹ Ph.D. Candidate, Dept. of Aerospace Engineering, 0245 Howe Hall, ying@iastate.edu, AIAA student member.

² Professor of Aerospace Engineering, 2271 Howe Hall, zjw@iastate.edu, Associate Fellow of AIAA.

and appropriate boundary conditions on $\partial\Omega$. In (2.1), x, y , and z are the Cartesian coordinates and $(x, y, z) \in \Omega$, $t \in [0, T]$ denotes time. Q is the vector of conserved variables, and F, G and H are the fluxes in the x, y and z directions, respectively, which take the following form

$$Q = \begin{pmatrix} \rho \\ \rho u \\ \rho v \\ \rho w \\ E \end{pmatrix} \quad (2.1c)$$

$$F = F^i - F^v = \begin{pmatrix} \rho u \\ \rho u^2 + p \\ \rho uv \\ \rho uw \\ (E + p)u \end{pmatrix} - \begin{pmatrix} 0 \\ \tau_{xx} \\ \tau_{xy} \\ \tau_{xz} \\ u\tau_{xx} + v\tau_{xy} + w\tau_{xz} - q_x \end{pmatrix} \quad (2.1d)$$

$$G = G^i - G^v = \begin{pmatrix} \rho v \\ \rho uv \\ \rho v^2 + p \\ \rho vw \\ (E + p)v \end{pmatrix} - \begin{pmatrix} 0 \\ \tau_{xy} \\ \tau_{yy} \\ \tau_{yz} \\ u\tau_{xy} + v\tau_{yy} + w\tau_{yz} - q_y \end{pmatrix} \quad (2.1e)$$

$$H = H^i - H^v = \begin{pmatrix} \rho w \\ \rho uw \\ \rho vw \\ \rho w^2 + p \\ (E + p)w \end{pmatrix} - \begin{pmatrix} 0 \\ \tau_{xz} \\ \tau_{yz} \\ \tau_{zz} \\ u\tau_{xz} + v\tau_{yz} + w\tau_{zz} - q_z \end{pmatrix} \quad (2.1f)$$

where

$$\begin{aligned} E &= \frac{p}{\gamma - 1} + \frac{1}{2}\rho(u^2 + v^2 + w^2) \\ \tau_{xx} &= 2\mu \frac{\partial u}{\partial x} - \frac{2}{3}\mu \left(\frac{\partial u}{\partial x} + \frac{\partial v}{\partial y} + \frac{\partial w}{\partial z} \right) \\ \tau_{yy} &= 2\mu \frac{\partial v}{\partial y} - \frac{2}{3}\mu \left(\frac{\partial u}{\partial x} + \frac{\partial v}{\partial y} + \frac{\partial w}{\partial z} \right) \\ \tau_{zz} &= 2\mu \frac{\partial w}{\partial z} - \frac{2}{3}\mu \left(\frac{\partial u}{\partial x} + \frac{\partial v}{\partial y} + \frac{\partial w}{\partial z} \right) \\ \tau_{xy} &= \mu \left(\frac{\partial u}{\partial y} + \frac{\partial v}{\partial x} \right), \tau_{xz} = \mu \left(\frac{\partial u}{\partial z} + \frac{\partial w}{\partial x} \right), \tau_{yz} = \mu \left(\frac{\partial v}{\partial z} + \frac{\partial w}{\partial y} \right) \end{aligned}$$

Coordinate transformation

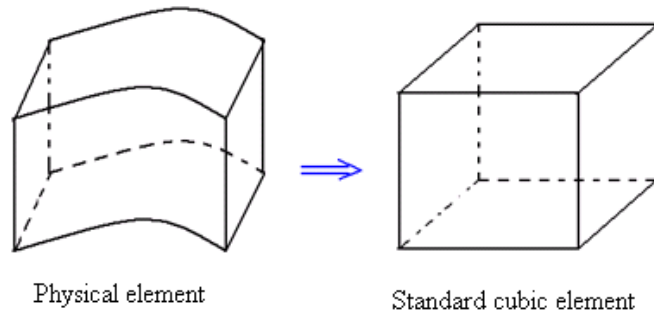


Figure 1. Transformation from a physical element to a standard element

In the SD method, it is assumed that the computational domain is divided into non-overlapping unstructured hexahedral cells or elements. In order to handle curved boundaries, both linear and quadratic isoparametric elements are employed, with linear elements used in the interior domain and quadratic elements used near high-order curved boundaries. In order to achieve an efficient implementation, all physical elements (x, y, z) are transformed into standard cubic element $(\xi, \eta, \zeta) \in [-1, 1] \times [-1, 1] \times [-1, 1]$ as shown in Figure 1.

The transformation can be written as

$$\begin{bmatrix} x \\ y \\ z \end{bmatrix} = \sum_{i=1}^K M_i(\xi, \eta, \varsigma) \begin{bmatrix} x_i \\ y_i \\ z_i \end{bmatrix} \quad (2.2)$$

where K is the number of points used to define the physical element, (x_i, y_i, z_i) are the Cartesian coordinates of these points, and $M_i(\xi, \eta, \varsigma)$ are the shape functions. For the transformation given in (2.2), the Jacobian matrix J takes the following form

$$J = \frac{\partial(x,y,z)}{\partial(\xi,\eta,\varsigma)} = \begin{bmatrix} x_\xi & x_\eta & x_\varsigma \\ y_\xi & y_\eta & y_\varsigma \\ z_\xi & z_\eta & z_\varsigma \end{bmatrix}.$$

The governing equations in the physical domain are then transformed into the standard element, and the transformed equations take the following form

$$\frac{\partial \tilde{Q}}{\partial t} + \frac{\partial \tilde{F}}{\partial \xi} + \frac{\partial \tilde{G}}{\partial \eta} + \frac{\partial \tilde{H}}{\partial \varsigma} = 0 \quad (2.3)$$

where

$$\begin{bmatrix} \tilde{F} \\ \tilde{G} \\ \tilde{H} \end{bmatrix} = |J| \begin{bmatrix} \xi_x & \xi_y & \xi_z \\ \eta_x & \eta_y & \eta_z \\ \varsigma_x & \varsigma_y & \varsigma_z \end{bmatrix} \cdot \begin{bmatrix} F \\ G \\ H \end{bmatrix}$$

Spatial Discretization

In the standard element, two sets of points are defined, namely the solution points and the flux points, illustrated in Figure 2 for a 2D element. The solution unknowns (conserved variables Q) or degrees-of-freedom (DOFs) are stored at the solution points, while fluxes are computed at the flux points. The solution points in 1D are chosen to be the Gauss points defined by

$$X_s = \cos\left(\frac{2s-1}{2N} \cdot \pi\right), s = 1, 2, \dots, N. \quad (2.4)$$

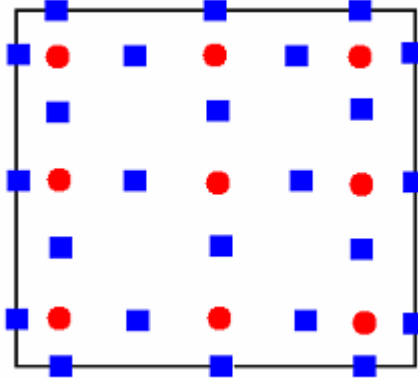


Figure 2. Distribution of solution points (circles) and flux points (squares) in a standard element for a 3rd-order SD scheme.

With solutions at N points, we can construct a degree $(N - 1)$ polynomial in each coordinate direction using the following Lagrange basis defined as

$$h_i(X) = \prod_{s=1, s \neq i}^N \left(\frac{X - X_s}{X_i - X_s} \right) \quad (2.5)$$

The reconstructed solution for the conserved variables in the standard element is just the tensor products of the three one-dimensional polynomials, i.e.,

$$Q(\xi, \eta, \varsigma) = \sum_{k=1}^N \sum_{j=1}^N \sum_{i=1}^N \frac{\tilde{Q}_{i,j,k}}{|J_{i,j,k}|} h_i(\xi) \cdot h_j(\eta) \cdot h_k(\varsigma) \quad (2.6)$$

The flux points in 1D are chosen to be the $(N - 1)$ Gauss quadrature points plus the two ending points. With

fluxes at $(N + 1)$ points, a degree N polynomial can be constructed in each coordinate direction using the following Lagrange bases defined as

$$l_{i+1/2}(X) = \prod_{s=0, s \neq i}^N \left(\frac{X - X_{s+1/2}}{X_{i+1/2} - X_{s+1/2}} \right) \quad (2.7)$$

Similarly, the reconstructed flux polynomials take the following form:

$$\tilde{F}(\xi, \eta, \varsigma) = \sum_{k=1}^N \sum_{j=1}^N \sum_{i=0}^N \tilde{F}_{i+1/2,j,k} l_{i+1/2}(\xi) \cdot h_j(\eta) \cdot h_k(\varsigma) \quad (2.8a)$$

$$\tilde{G}(\xi, \eta, \varsigma) = \sum_{k=1}^N \sum_{j=0}^N \sum_{i=1}^N \tilde{G}_{i,j+1/2,k} h_i(\xi) \cdot l_{j+1/2}(\eta) \cdot h_k(\varsigma) \quad (2.8b)$$

$$\tilde{H}(\xi, \eta, \varsigma) = \sum_{k=0}^N \sum_{j=1}^N \sum_{i=1}^N \tilde{H}_{i,j,k+1/2} h_i(\xi) \cdot h_j(\eta) \cdot l_{k+1/2}(\varsigma) \quad (2.8c)$$

Because the SD method is based on the differential form of the governing equations, the implementation is straightforward even for high-order curved boundaries. All the operations are basically one-dimensional in each coordinate direction and each coordinate direction shares the collocated solution points with others, resulting in improved efficiency. In summary, the algorithm to compute the inviscid flux and viscous flux and update the unknowns (DOFs) consists the following steps:

1. Given the conserved variables $\{Q_{i,j,k}\}$ at the solution points, compute the conserved variables $\{Q_{i+1/2,j,k}\}$ at the flux points using polynomial (2.6).
2. Note that inviscid flux is a function of the conserved solution and the viscous flux is a function of both the conserved solution and its gradient, taking flux \tilde{F} for example:

$$\begin{cases} \tilde{F} = \tilde{F}^i - \tilde{F}^v \\ \tilde{F}_{i+1/2,j,k}^i = \tilde{F}^i(Q_{i+1/2,j,k}) \\ \tilde{F}_{i+1/2,j,k}^v = \tilde{F}^v(Q_{i+1/2,j,k}, \nabla Q_{i+1/2,j,k}) \end{cases} \quad (2.9)$$

Compute the inviscid fluxes $\{\tilde{F}_{i+1/2,j,k}^i\}$ at the interior flux points using the solution $\{Q_{i+1/2,j,k}\}$ computed at Step 1. Compute the viscous fluxes $\{\tilde{F}_{i+1/2,j,k}^v\}$ using the solution $\{Q_{i+1/2,j,k}\}$ computed at Step 1 and the gradient of the solutions $\{\nabla Q_{i+1/2,j,k}\}$ computed based on $\{Q_{i+1/2,j,k}\}$.

3. Compute the common inviscid flux at element interfaces using a Riemann solver (2.11), such as the Roe solver and Rusanov solver¹³.

$$\tilde{F}^i = \tilde{F}^i(Q_L, Q_R) \quad (2.11)$$

where Q_L and Q_R represent the solutions from the two elements beside the interface.

Compute the common viscous flux at element interfaces using a viscous approach (2.12), such as the averaged approach and DG-like approach¹³.

$$\tilde{F}^v = \tilde{F}^v(Q_L, Q_R, \nabla Q_L, \nabla Q_R) \quad (2.12)$$

Then compute the derivatives of the fluxes at all the solution points by using (2.13).

$$\left(\frac{\partial \tilde{F}}{\partial \xi} \right)_{i,j,k} = \sum_{r=0}^N \tilde{F}_{r+1/2,j,k} l'_{r+1/2}(\xi_i) \quad (2.13a)$$

$$\left(\frac{\partial \tilde{G}}{\partial \eta} \right)_{i,j,k} = \sum_{r=0}^N \tilde{G}_{i,r+1/2,k} l'_{r+1/2}(\eta_j) \quad (2.13b)$$

$$\left(\frac{\partial \tilde{H}}{\partial \varsigma} \right)_{i,j,k} = \sum_{r=0}^N \tilde{H}_{i,j,r+1/2} l'_{r+1/2}(\varsigma_k) \quad (2.13c)$$

4. Update the DOFs using a multistage TVD scheme for time integration of (2.14).

$$\frac{\partial \tilde{Q}_{i,j,k}}{\partial t} = - \left(\frac{\partial \tilde{F}}{\partial \xi} + \frac{\partial \tilde{G}}{\partial \eta} + \frac{\partial \tilde{H}}{\partial \varsigma} \right)_{i,j,k} \quad (2.14)$$

For more details about SD method on hexahedral mesh, the readers can refer to¹³.

III. Simulation Results

Computational grid

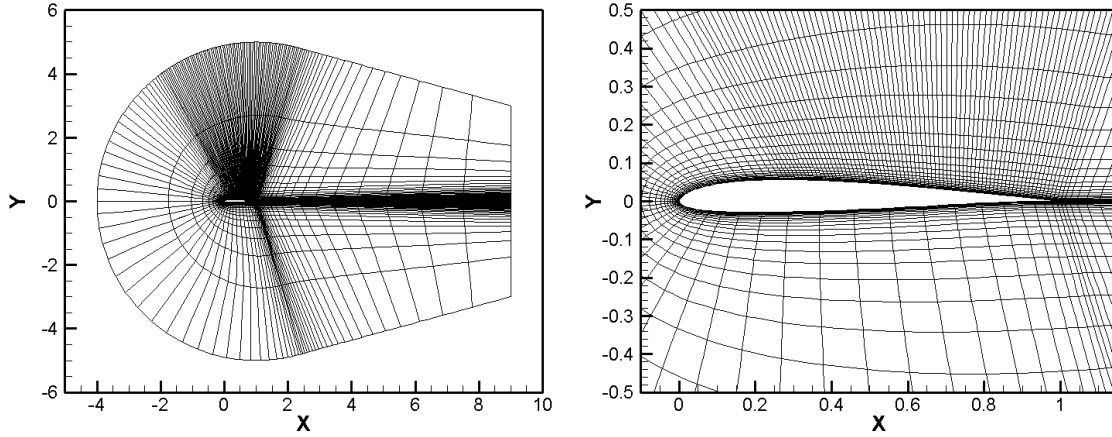


Figure 3. Computational mesh

Figure 3 shows the computational grid for the current ILES simulation. Refined mesh is designed to concentrate near the wall and around the physically important region where the separation bubble and vortex breakdown happens. The smallest cells are located at the trailing edge corners with dimension (in wall units) $\Delta y^+ = 2.5$ in the direction normal to the wall, $\Delta x^+ = 25.0$ along the chord and $\Delta z^+ = 12.0$ in spanwise direction. The total number of elements used here is 78,500, resulting 2,119,500 and 5,024,000 degree-of-freedom (per equation) for 3rd-order and 4th-order SD method respectively.

For the infinite wing assumption, the periodic boundary condition is used in spanwise direction and the span width of the wing is set to be 20% of the chord which was proved to be wide enough in ¹⁵. At the far-field of the computational domain, a full-state type boundary condition is imposed. And a non-slip, adiabatic boundary condition is applied on the surface of the airfoil.

Averaged and statistical results

The increasing interest on MAV is in the low-Mach-number and low-Reynolds-number regime, and many experimental measurements were conducted under incompressible flow conditions. In the present study with the SD method and compressible Navier-Stokes equations, computations are performed at an incoming Mach number of 0.2. To verify that this Mach number is low enough, a solution with an inflow Mach number of 0.1 is also presented here. In Figure 4, the mean pressure coefficient $C_p = (p - p_\infty)/\frac{1}{2}\rho_\infty U_\infty^2$ and mean skin friction coefficient $C_f = \tau/\frac{1}{2}\rho_\infty U_\infty^2$ on the wing surface of both cases using the 3rd-order SD method are compared and little difference has been found. In this paper, the mean flow field and the statistical results are obtained by averaging the instantaneous flow field at each time step and performed over a non-dimensional time $t = t^*/(C/U_\infty)$ interval of $\Delta t = 8.0$. The mean pressure coefficient at Mach number 0.1 is also compared with the result obtained by Galbraith et al.¹⁵ in Figure 5 and good agreement has been found. Therefore, Mach number 0.2 is concluded a satisfactorily low Mach number and used for all remaining computations.

A polynomial order (p) refinement study is carried out by increasing the order of the polynomial in each element cell from 2 (resulting in 3rd-order accuracy) to 3 (resulting in 4th-order accuracy). Very good agreement between the 3rd-order method and 4th-order method has been found in Figure 6 for both the mean pressure coefficient and mean skin friction coefficient on the wing surface, thus indicating that the converged mean flow has been achieved and the spatial resolution provided by 4th-order method is capable to capture the main flow features at this Reynolds number.

Table 1 compares the locations of separation, transition and reattachment between the 3rd-order and the 4th-order results. The onset location of transition is defined by a critical value of 0.001 of the normalized Reynolds stress widely used in ¹⁵⁻²⁰. The differences between the above measurements of the 3rd-order and the 4th-order results are all less than 2%. The results from Galbraith et al.¹⁵ are also listed here and the agreement here is also good.

Table 1. Separation, transition and reattachment locations

Case	Separation	Transition	Reattachment
3 rd -order	0.223	0.515	0.675
4 th -order	0.227	0.521	0.685
Galbraith et al. ¹⁵	0.23	0.55	0.65

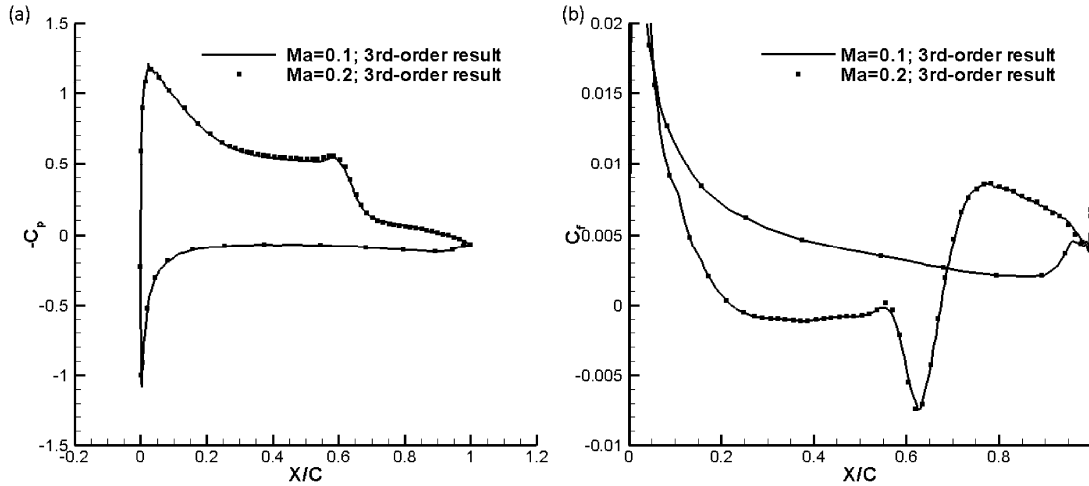


Figure 4. Mean pressure coefficient C_p (a) and mean skin friction coefficient C_f (b) on the wing surface. Solid line: $Ma=0.1$; square symbols: $Ma=0.2$.

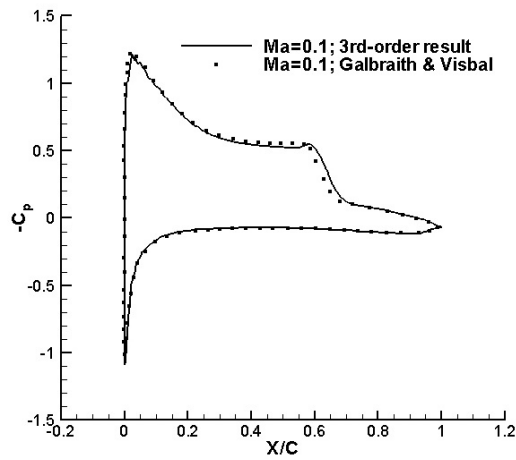


Figure 5. Mean pressure coefficient C_p on the wing surface with comparison to the computations by previously published results. Solid line: 3rd-order SD results; square symbols: Galbraith et al.¹⁵

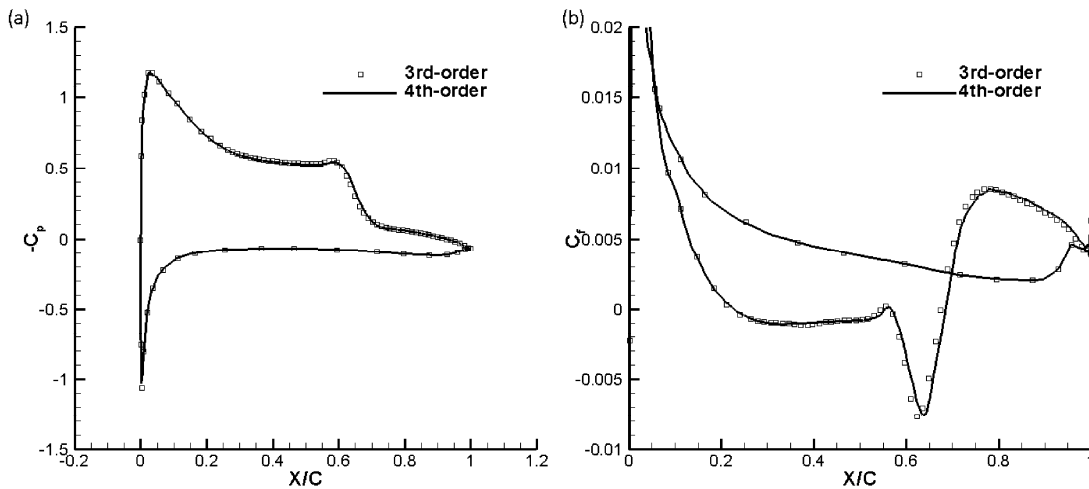


Figure 6. Mean pressure coefficient C_p (a) and mean skin friction coefficient C_f (b) on the wing surface. Square symbols: 3rd-order result; solid line: 4th-order result.

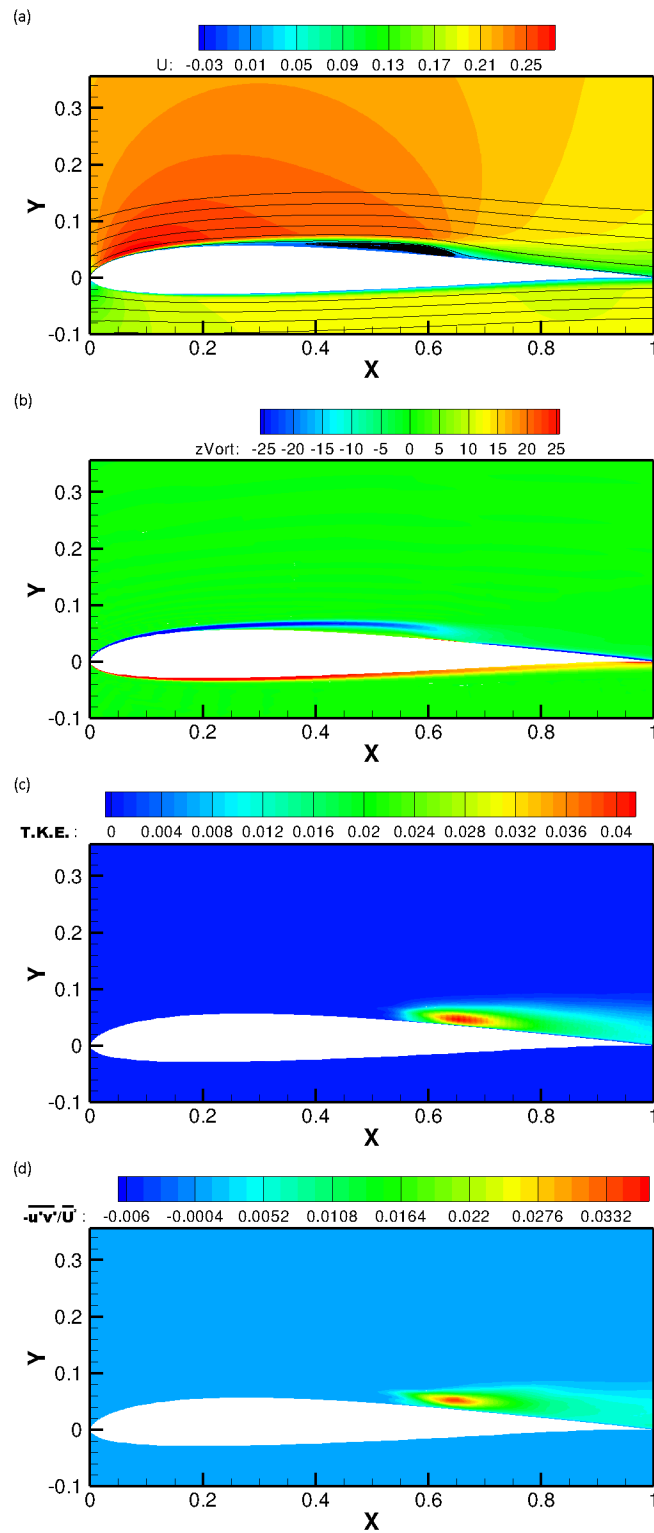


Figure 7. Mean and statistical results: (a) mean streamlines around the wing and mean streamwise velocity field; (b) mean spanwise vorticity field; (c) normalized turbulent kinetic energy (*T.K.E.*) distribution; (d) normalized Reynolds stress (τ_{xy}) distribution.

Figure 7.a shows the mean streamlines around the wing and the mean streamwise velocity field averaged in both time and spanwise direction. The mean separation bubble and the reattachment of the flow are clearly shown. In Figure 7.b, the low value of the mean spanwise vorticity on the suction surface of the wing at interval $x = [0.0, 0.6]$ represents the laminar shear layer before the flow transits to turbulent. The amplitude of disturbance during this interval has been found to grow exponentially due to the boundary layer instability before separation and the Kelvin-Helmholtz instability after separation¹⁹⁻²¹. The shear layer ends around $x = 0.65$ at the end of the LSB (Figure 7.a) where the vortex breakdown happens. A turbulent boundary layer forms at interval $x = [0.75, 1.0]$ thereafter. Figure 7.c and d show the statistical distribution of the normalized turbulent kinetic energy ($T.K.E. = \frac{1}{2}(\overline{u'^2} + \overline{v'^2} + \overline{w'^2})$) and the normalized Reynolds stress ($\tau_{xy} = -\overline{u'v'}/U_\infty^2$), respectively. The concentration of both the normalized $T.K.E.$ and Reynolds stress around $x \approx 0.65$ is strongly related to the process of vortex breakdown, and is discussed in the following section.

Figure 8 shows the mean flow field velocity profiles in direction normal to the wall along the chord line. Profiles are extruded in the wall's normal direction at each chord location. The evolvement of the velocity profile from an attached boundary layer to a detached one is clearly shown. The strong shear layer where the gradient of the velocity is big detaches away from the wall gradually (dashed line) and the thickness of the shear layer grows in the chord line. The separation of the flow appears after $x = 0.25$.

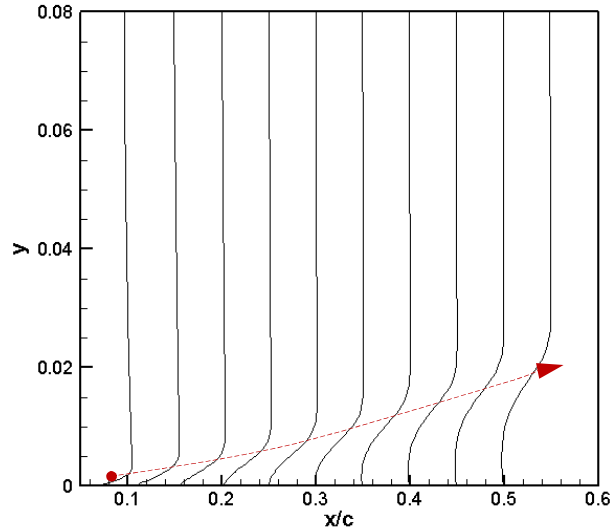


Figure 8. Mean flow field profiles at $x = 0.1 \sim 0.5$

IV. Transition Process and Mechanism

The transition from the laminar flow to turbulent flow usually experiences a process of the growth of the initial disturbances inside the laminar flow and vortex breakdown after the disturbances reach a certain level²³. In this section, the authors try to investigate and discuss the process and mechanism of the separated and transitional flow over the SD7003 wing.

The original disturbances

In the current paper and previously published papers^{15, 20} for the same case, no incoming disturbances are introduced at the inlet boundaries. However, the transition process happens and is self-sustained once the turbulent flow forms over the wing and propagates to the trailing edge, also shown in^{15, 20}. Figure 9 shows the pressure spectrums at $x = 0.1 \sim 0.3$ and different y locations inside the boundary layer. At the same x location the low frequency part ($\omega < 0.2$) is different, while the high frequency part ($\omega \geq 0.2$) of the pressure spectrums at three different y locations is nearly on top of each other. The spectrum shapes of the high frequency part at different x locations are also quite similar.

By using a Fourier transform and inverse Fourier transform with a window filter, the high frequency part ($\omega \geq 0.2$) is extracted out. Figure 10 shows the histories of the original pressure disturbances (Figure 10.a) and the extracted high frequency part (Figure 10.b). It is found that the wave shapes and amplitudes of the high frequency part are nearly the same at three different locations $x = 0.1, 0.2, 0.3$ and the wave is actually from downstream to

upstream (Figure 10.b). It is reasonable to conclude that the high frequency part is due to the aeroacoustic signal. The aeroacoustic noise is mainly generated near the trailing edge and propagates upstream as in a subsonic problem. The low frequency part is also thought to contain the aeroacoustic signal, but cannot be extracted out here. The upstream propagating acoustic noise plays as the main source of the initial disturbances to trigger the transition and keep the transitional process self-sustained even though no incoming disturbances are introduced. The low frequency part is thought to be the unstable T-S wave and discussed in the following subsection.

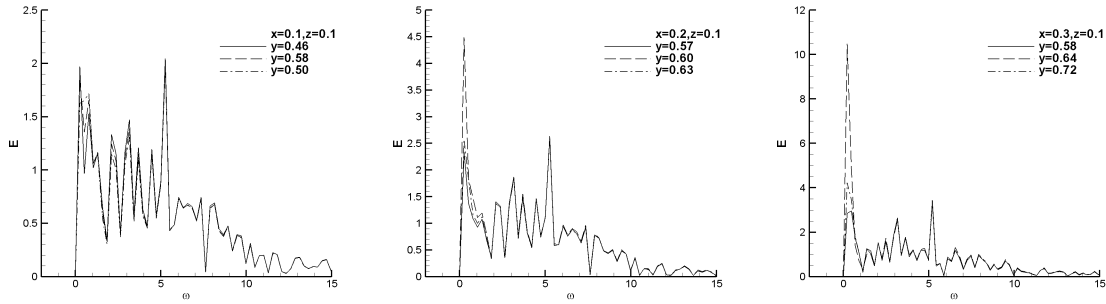


Figure 9. Spectrum of pressure at $x = 0.1 \sim 0.3$

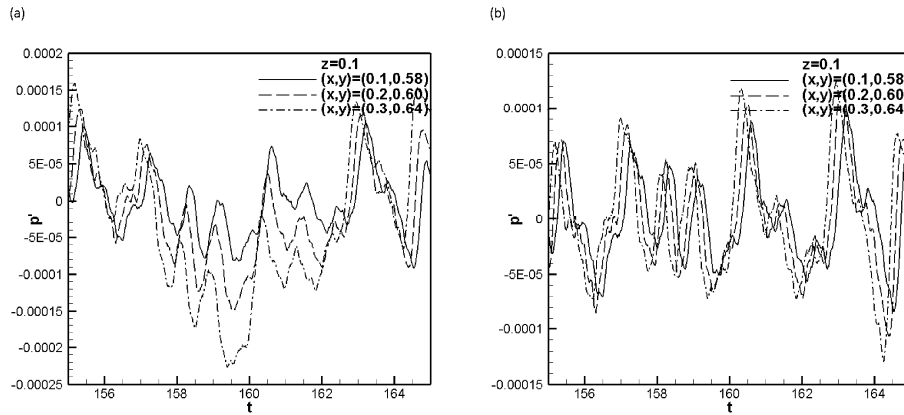


Figure 10. Pressure disturbances history (a) and the filtered high pressure part (b) in time interval $t = 155 \sim 165$

Growth of the disturbances

Usually the disturbances in a laminar flow need to grow and reach certain levels before transition can happen²³. In the current case, an overall exponential growth of the disturbances is observed before transition. In²⁰, it was found that at $x = 0.1 \sim 0.5$ the overall disturbances keep growing exponentially and the shapes of the disturbance profile look like a typical T-S wave in $x = 0.1 \sim 0.3$. The results in this paper agree well with the observation in²⁰, and the dominant disturbances are found to be of low frequency before the vortex shedding and of high frequency thereafter. Figure 11 shows the spectrums of u-velocity at different locations from the leading edge to the transition onset location, $x = 0.1 \sim 0.6$. A low frequency part ($\omega < 0.2$) dominates the spectrum in $x = 0.1 \sim 0.4$ and keeps growing, but a higher frequency part ($4.0 < \omega < 15.0$) becomes more and more dominant in $x = 0.4 \sim 0.6$.

After $x = 0.3$, the boundary layer separates and the inflection point appears. The Kelvin-Helmholtz type of inviscid instability takes the dominant role in the disturbance growth and the low frequency disturbance could not sustain. The vortices shed out in the detached shear layer during the interval $x = 0.3 \sim 0.4$ (Figure 12). The size of the vortices grows gradually after shedding and before transition. The shedding frequency of the vortex is not a single one but in the continuous band which corresponds to the dominant frequency band ($4.0 < \omega < 9.0$) in the spectrums of $x = 0.4 \sim 0.6$. The dominant frequency band agrees well with the predictions of the linearized stability theory (LST) though the mean profile violates the assumption of parallel flow in LST. Figure 13 shows the unstable mode at $x = 0.3, 0.4, 0.5$ based on LST with the mean profiles. The unstable region is about $0.0 \leq \omega \leq 15$ for all three locations and it is shown in the spectrums of u-velocity that only the part $0.0 \leq \omega \leq 15$ is excited, and the part

$\omega > 15$ is stable and remains unexcited. In Figure 11, the flow is found to be more unstable in $4.0 \leq \omega \leq 9.0$. In the spectrums, the part in $4.0 \leq \omega \leq 9.0$ gradually dominates the spectrums after $x = 0.4$. Another main part $10.0 \leq \omega \leq 15.0$ is also observed in the spectrums after $x = 0.4$ and it might be the double harmonic waves excited by the fundamental waves of $4.0 \leq \omega \leq 9.0$. The part $\omega > 15.0$ of the double harmonic waves exceeds the unstable region predicted by LST and is not excited.

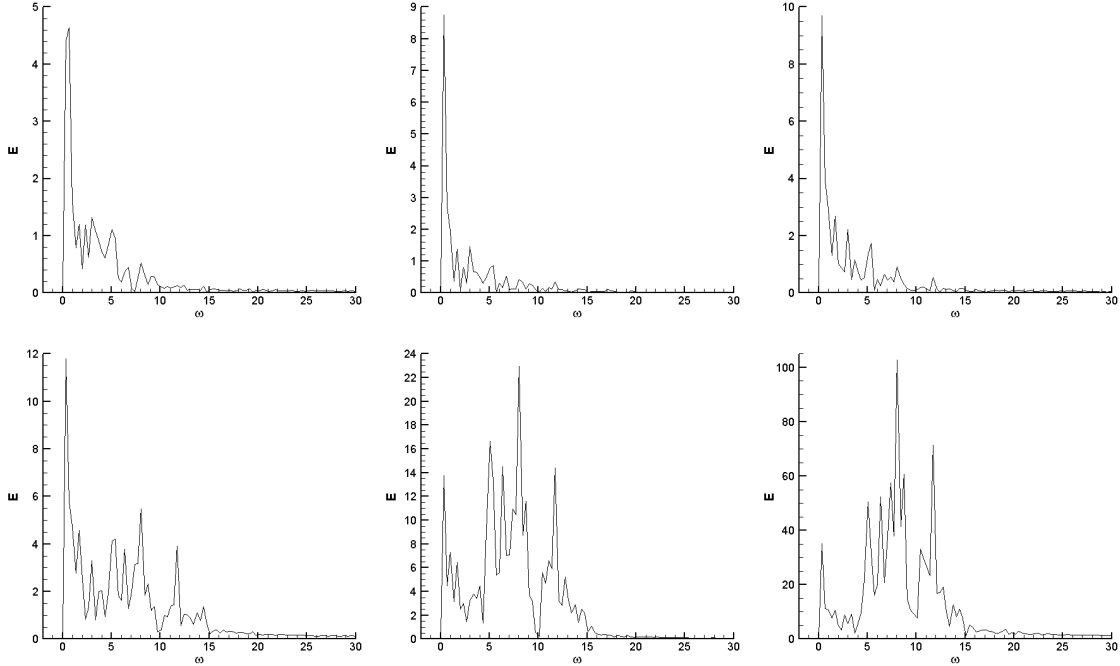


Figure 11. Spectrum of u-velocity at $x = 0.1 \sim 0.6$

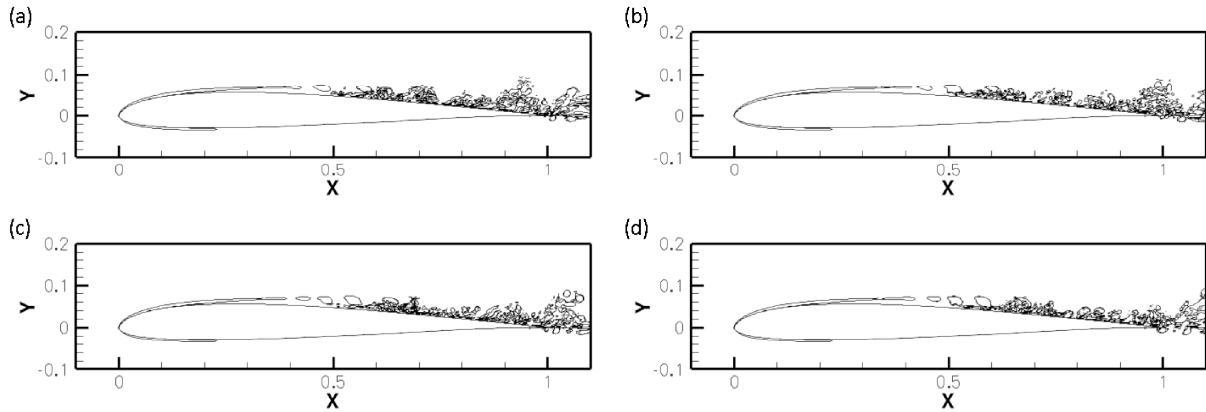


Figure 12. Instantaneous contour line of $Q = 1$ at time $t = 155.32 \sim 156.44$

Figure 14 shows the disturbances amplitude of pressure and v-velocity at $x = 0.1 \sim 0.6$ and $z = 0.1$. The disturbances amplitude is defined as $A(x) = \overline{v(x, y, t)^2}$ & $\overline{p(x, y, t)^2}$ for v-velocity and pressure respectively, and the average is taken in both y-direction and time. The averaged and statistical results are achieved based on 20 probe points, which are equally placed inside the boundary layer as the disturbances mainly exist inside the shearing boundary layer. In Figure 14, the vertical coordinate is set to be the logarithm of the disturbance amplitude normalized by the disturbance amplitude of the first location $x = 0.1$. The solid line in Figure 14.a for v-velocity shows a linear increase in $x = 0.1 \sim 0.6$ representing an exponential growth of the overall v-velocity disturbance which agrees well with result in ²⁰. The disturbances amplitude of the low frequency part ($\omega < 0.2$) and the rest frequency part (mainly $4.0 < \omega < 15.0$) are also presented here. It is clearly shown there that the low frequency part is dominant and responsible for the exponential growth of the overall disturbances in the early stage $x =$

0.1 ~ 0.3, while the higher frequency part takes over the dominant role in the exponential growth of the overall disturbances in the later stage $x = 0.5 \sim 0.6$. In the interval where $x = 0.3 \sim 0.5$, a transient process happens where the growth of the low frequency part slows down but the growth of the high frequency part increases quickly. The interval $x = 0.3 \sim 0.4$ corresponds to the region where the shedding of the vortices happens as discussed before. In this interval the disturbance energy is transported from the low frequency disturbances to higher frequency disturbances through the vortex shedding. The disturbance amplitude of pressure also shows a similar trend (Figure 14.b). However, the overall pressure disturbance does not show an exponential growth which is due to the acoustic noises existing in the flow field.

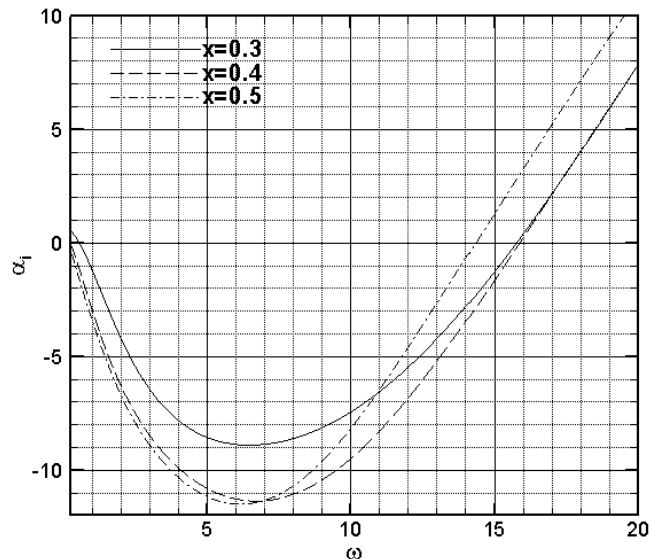


Figure 13. Unstable modes at $x = 0.3, 0.4, 0.5$ based on LST

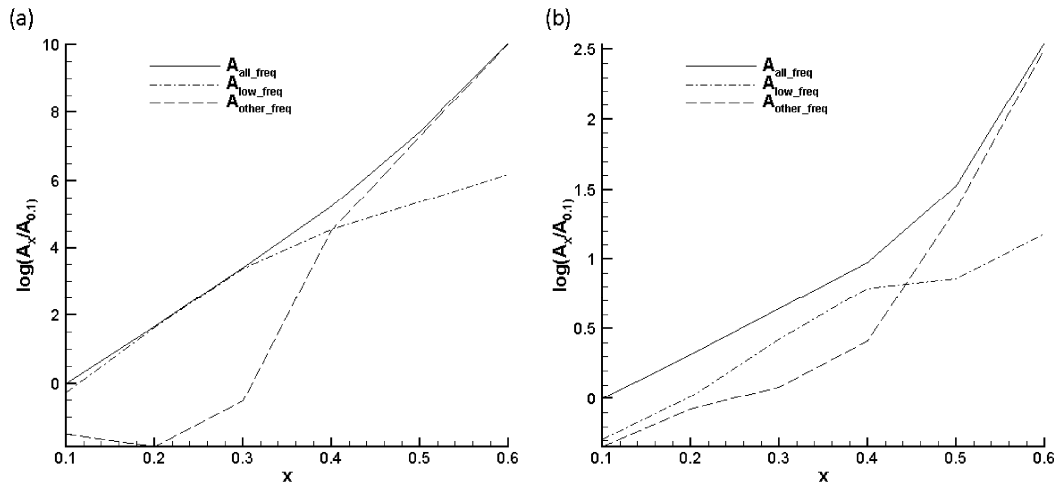


Figure 14. Disturbances amplitude of v-velocity (a) and pressure (b) at $x = 0.1 \sim 0.6$

Breakdown of the shedding vortices

A LSB forms after the flow separates and two dimensional vortices shed. The LSB in the current case can be classified as a long one according to the classification in ²². It is observed that the quasi two dimensional vortex break down to small scale structures during the interval $x = 0.55 \sim 0.75$, as shown in Figure 12. This interval corresponds to the transition onset region, where the skin friction and the wall pressure increase suddenly. It is observed in Figure 12 that the shedding vortex breakdown process carries gradually from the bottom to the top and the small scale structures attaching to the wall at $x = 0.5 \sim 0.6$ with negative u-velocity play an important role. A thin layer of small scale structures stay near the wall at $x = 0.5 \sim 0.6$ right below the shedding vortex. As the thin

layer stays inside the separation bubble, the small scale structures move upstream with small negative u-velocity and then are upcasted by the circulation of the separated flow. When the shedding vortex propagates pass the region, the bottom part of the shedding vortex meets and interacts with the upstream going small scale structures. The bottom part of the vortex breaks down to small scale structures first, then the upper part of the vortex is gradually affected and breaks down by the spin of the vortex itself. In this way, the vortex tube breaks down from the bottom to the top. Figure 15 shows the w-velocity history at the three different y locations with the same chord location $x = 0.6$. Three points are put equally spaced inside the mean shear layer. The w-velocity history near the wall is highly oscillatory while away from the wall it remains close to zero. This also indicates that the shedding vortices are three dimensional small scale structures at the bottom but quasi two-dimensional large structures at the top during the breakdown process at $x = 0.6$. After the breakdown of the large scale vortex into small scale eddies, the flow becomes more and more turbulent and propagates downstream.

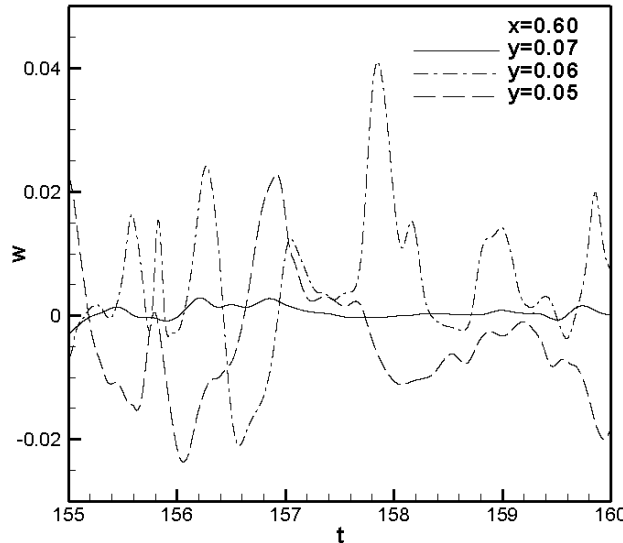
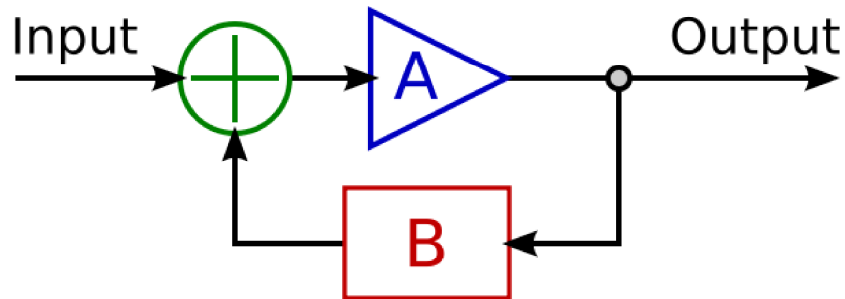


Figure 15. w-velocity history at time interval $t = 155 \sim 160$



Input: shedding vortices due to Kevin-Helmholtz instability

Output: reattached turbulent boundary layer

A: breakdown of the vortices

B: small scale structures attached on the wall with negative velocities

Figure 16. The negative feedback mechanism in breakdown of the flow over SD7003

The traditional description of the separation-transition-reattachment type of flow is as follows: the flow separates and transitions to turbulent then reattaches to the wall downstream¹⁹. Here, a hypothesis of a negative feedback mechanism is proposed and supplements the traditional description for this particular case. In the current case, the transition onset and the vortex breakdown are caused not only by the growth and evolution of the original disturbances but also the upstream-propagating small scale structures. The origin of the small scale structures is from the turbulent flow after breakdown. The feedback loop is connected by the upstream-propagating small scale

structures with negative u-velocity as shown in Figure 16.

The negative feedback is also called a balance loop. The instantaneous transition point is balancing back and forth around the mean transition point and does not move further upstream or downstream with the negative feedback. Two-dimensional shedding vortices and upstream going small scale structures are the two key essential factors in the transition with the separation bubble. The transition occurs where the two dimensional shedding vortices grow big enough and the upstream-propagating small scale structures are strong enough to trigger the vortex breakdown. So the transition does not happen further downstream. And the transition does not happen further upstream because the amplitude of the shedding vortices are not big enough and the strength and velocity of the upstream going small scale structures decay on the way upstream.

The turbulent vortical packet

After the vortex breakdown, the flow reattaches to the wall and forms a turbulent boundary layer. Individual turbulent vortical packets are found to form in the region $x = 0.6 \sim 0.7$ and propagate downstream after formation. As shown in both Figure 12 and 17, during the time interval $t = 155.32 \sim 157.56$ a turbulent vortical packet, noted by the dashed circle in Figure 17, develops gradually after breakdown. The mean u-velocity in the region $x = 0.6 \sim 0.7$ is low and close to zero (Figure 7.a). The shedding vortex breaks down around this region and the vortical packet forms and moves very slowly downstream. It is observed that more upstream shedding vortices reaching this region breaks down and joins the current vortical packet. The shedding vortices merge together and the turbulent vortical packet becomes bigger and stronger. Actually, the almost non-moving turbulent packet provides the upstream-propagating small scale structures which cause the breakdown of the shedding vortices as described previously.

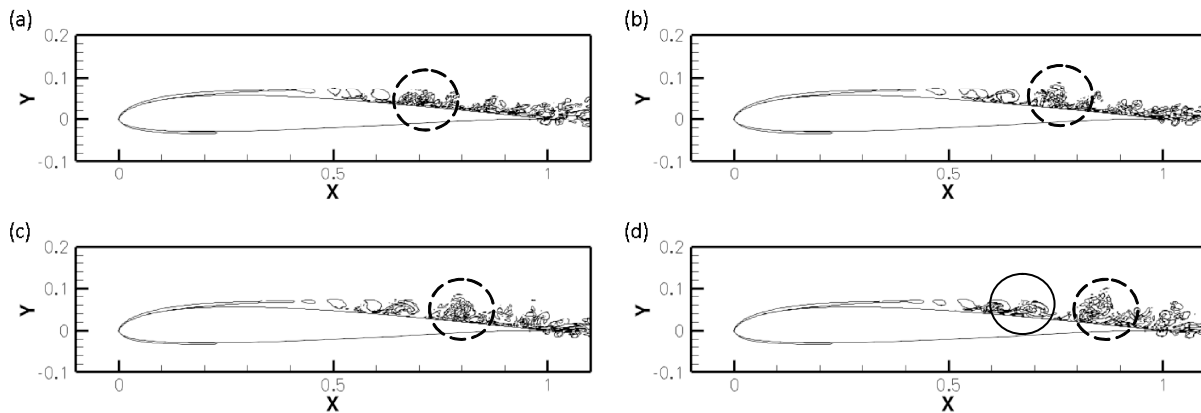


Figure 17. Instantaneous contour line of $Q = 1$ at time $t = 156.76 \sim 157.56$

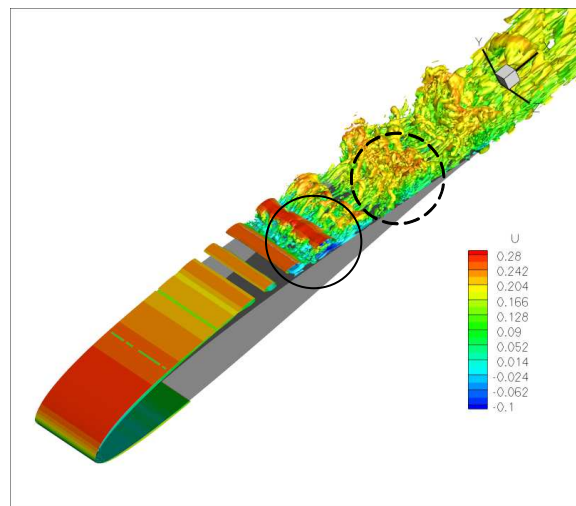


Figure 18. Iso-surface of Q-criterion colored by streamwise velocity at time $t = 157.56$

The characteristics of the pressure and skin friction on the wall are strongly associated with the formation of the turbulent packet. Figure 19 shows the instantaneous C_p and C_f during the time interval $t = 155.32 \sim 156.56$. The instantaneous C_f shows that a small separation region $x = 0.6 \sim 0.7$ nearly does not move during the time interval. Meanwhile, this region corresponds to the sudden jump of the instantaneous C_p (Figure 19.a). And this also accounts for the featured characters of the mean C_p and C_f as shown in Figure 20 and also in Figure 6.

The formation and evolution of the turbulent vortical packet are also responsible for the characters of the mean spanwise vorticity, the normalized $T.K.E.$ and the normalized Reynolds stress (τ_{xy}) as shown in Figure 7. The region $x = 0.6 \sim 0.7$ corresponds with the region where the separated shear layer ends (Figure 7.b), the source of T. K. E. (Figure 7.c) and the high concentration of the Reynolds stress (Figure 7.d).

After reaching certain strength, the turbulent vortical packet leaves the region $x = 0.6 \sim 0.7$ and propagates downstream (Figure 17). And a new turbulent vortical packet noted by the solid circle in Figure 17.d and 18 forms in the same region.

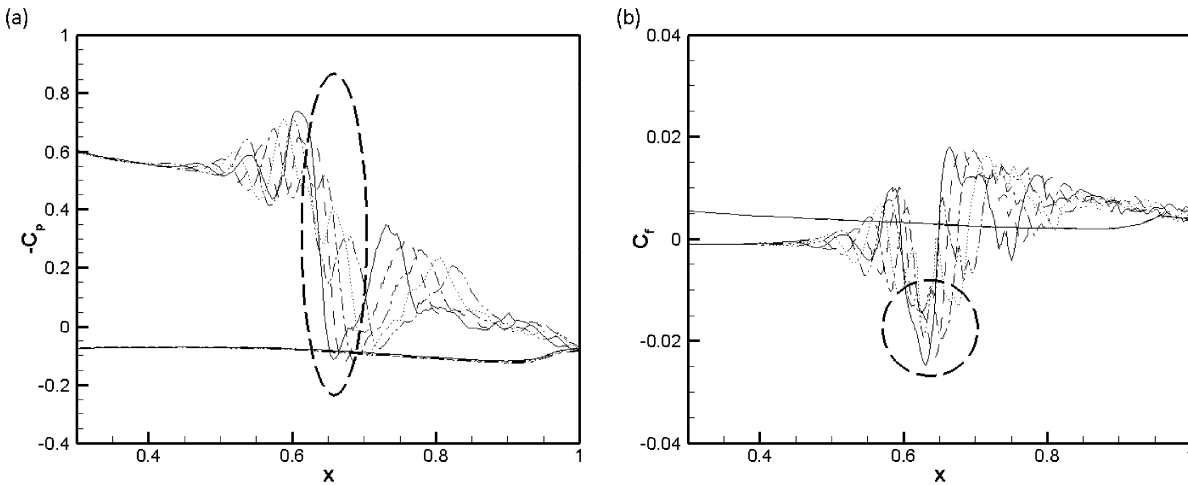


Figure 19. Instantaneous pressure coefficient C_p (a) and skin friction C_f (b) during the time interval $t = 155.32 \sim 156.56$

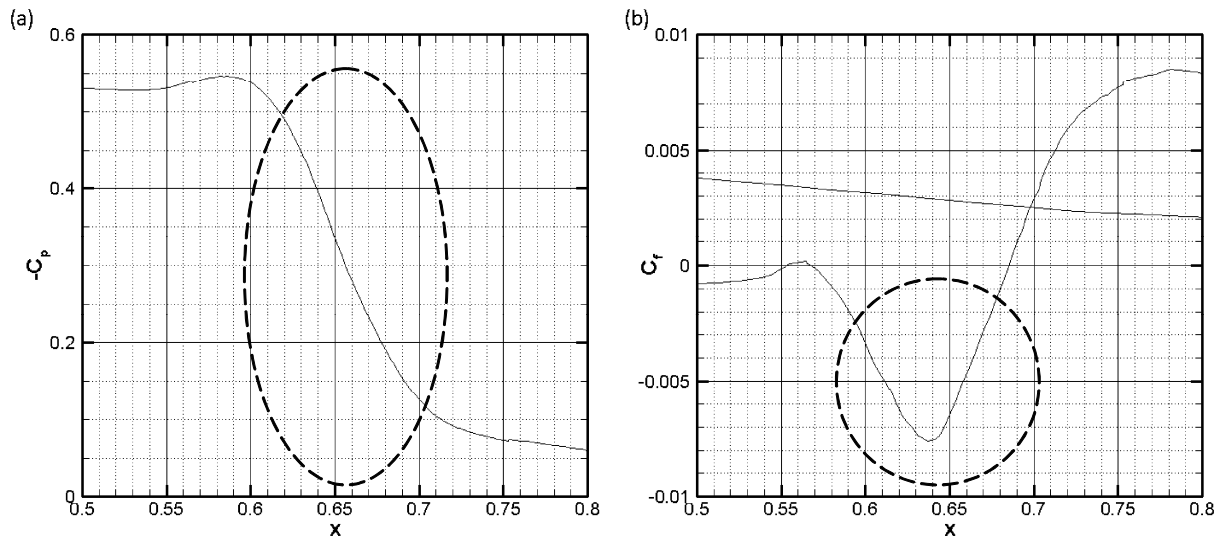


Figure 20. The zoom-in pressure coefficient C_p (a) and skin friction C_f (b) of Figure 6

V. Conclusion

The separated and transitional flow over a SD7003 wing is numerically investigated in this paper. The averaged and statistical results agree well with the previously published results and good agreement is also found in a p-type grid

refinement study. The SD method with unstructured hexahedral mesh together with ILES captures the LSB and the transition process well over the suction side of the wing.

The process and mechanism of the separation and the transitional flow are described and discussed. The acoustic noises are found to act as the original disturbances inside the laminar boundary layer. The disturbances grow exponentially inside the shear layer owing to the boundary layer T-S instability and then the Kelvin-Helmholtz instability. And the disturbances are found to be of low frequency before separation and of high frequency thereafter. Individual turbulent packets form after the breakdown and shedding vortices also merge to form larger ones. The turbulent packet moves slowly within the breakdown region and the small scale structures move upstream with the negative u-velocity inside the LSB. During the breakdown process of the shedding vortices, the upstream going small scale structures near the wall play an important role and a hypothesis of a negative feedback mechanism is proposed, which appears to be supported by an iso-Q movie.

Acknowledge

The authors would like to acknowledge the support for this work from the Department of Aerospace Engineering, Iowa State University, and partial support by the Air Force Office of Scientific Research.

References

- ¹Patera, A.T., A Spectral element method for fluid dynamics: Laminar flow in a channel expansion, *J. Comput. Phys.* 54, 468(1984).
- ²Kopriva, D.A. and Kalias, J.H., A conservative staggered –grid Chebyshev multidomain method for compressible flows, *J. Comput. Phys.* 125, 244(1996).
- ³D.A. Kopriva, J.H. Kalias, A Staggered-Grid Multidomain Spectral Method for the Compressible Navier-Stokes Equations, *J. Comput. Phys.* 143 (1998) 125-158.
- ⁴Barth, T.J. and Frederickson, P.O., High-Order Solution of the Euler Equations on Unstructured Grids using Quadratic Reconstruction, AIAA Paper No. 90-0013(1990).
- ⁵Hu, C. and Shu, C.-W., Weighted essentially non-oscillatory schemes on triangular meshes, *J. Comput. Phys.* 150, 97 (1999).
- ⁶Cockburn, B. and Shu, C.-W., TVB Runge-Kutta local projection discontinuous Galerkin finite element method for conservation laws II: General framework, *Math. Comput.* 52,411(1989).
- ⁷Abgrall, R. and Roe, P.L., High Order Fluctuation Schemes on Triangular Meshes, *Journal of Scientific Computing*, Volume 19, pp. 3 – 36, 2003.
- ⁸Wang, Z.J. and Liu, Yen, Spectral (Finite) Volume Method for Conservation Laws on Unstructured Grids III: Extension to One-Dimensional Systems, *J. Scientific Computing*, Vol. 20 No. 1, pp.137-157 (2004).
- ⁹Liu, Y., Vinokur, M., and Wang, Z.J., Discontinuous Spectral Difference Method for Conservation Laws on Unstructured Grids, in *Proceeding of the 3rd International Conference in CFD*, Toronto, Canada July 2004.
- ¹⁰Liu, Yen, Vinokur, M., and Wang, Z.J., Multi-Dimensional Spectral Difference Method for Unstructured Grids, AIAA-2005-0320.
- ¹¹Wang, Z. J., and Liu, Yen, The Spectral Difference Method for the 2D Euler Equations on Unstructured Grids, AIAA-2005-5112.
- ¹²Huang, P.G., Wang, Z.J., and Liu, Yen, An Implicit Space-Time Spectral Difference Method for Discontinuity Capturing Using Adaptive Polynomials, AIAA-2005-5255.
- ¹³Y. Sun, Z.J. Wang, Y. Liu, High-Order Multidomain Spectral Difference Method for the Navier-Stokes Equations on Unstructured Hexahedral Grids, *Communications in Computational Physics*, Vol. 2, No. 2(2007) 310-333.
- ¹⁴P. L. Roe, Approximate Riemann solvers, parameter vectors, and difference schemes, *J. Comput. Phys.* 43 (1981) 357-372.
- ¹⁵Galbraith, M. and Visbal, M., Implicit Large Eddy Simulation of low Reynolds number flow past the SD7003 airfoil," *Proc. of the 46th AIAA Aerospace Sciences Meeting and Exhibit*, Reno, Nevada, AIAA-2008-225, 2008.
- ¹⁶Volino, R. J., and Hultgren, L. S., 2001, "Measurements in Separated and Transitional Boundary Layers Under Low-Pressure Turbine Airfoil Conditions," *ASME J. Turbomach.*, 123, pp. 189 – 197.
- ¹⁷Oi, M. V., Hanff, E., McAuliffe, B., Scholz, U., and Kaehler, C., 2005, "Comparison of Laminar Separation Bubble Measurements on a Low Reynolds Number Airfoil in Three Facilities," 35th AIAA Fluid Dynamics Conference and Exhibit, Toronto, Ontario, June 6 – 9, AIAA Paper 2005-5149.
- ¹⁸Burgmann, S., Brucker, S., Schroder, W., 2006, "Scanning PIV Measurements of a Laminar Separation Bubble," *Exp. Fluids*, 41, pp. 319 – 326.
- ¹⁹Hu, H., Yang, Z.F., An Experimental Study of the Laminar Flow Separation on a Low-Reynolds-Number Airfoil, *MAY 2008*, Vol. 130 / 051101-1
- ²⁰Uranga, A., Persson P., Drela M. and Peraier J., Implicit Large Eddy Simulation of Transitional Flow Over Airfoils and Wings, 19th AIAA Computational Fluid Dynamics, San Antonio, Texas, June 22-25, AIAA 2009-4131.
- ²¹M. ALAM AND N. D. SANDHAM, Direct numerical simulation of 'short' laminar separation bubbles with turbulent reattachment, *J. Fluid Mech.* (2000), vol. 403, pp. 223-250.

²²Owen, P. R. and Klanfer, L. 1953, On the laminar boundary layer separation from the leading edge of a thin aerofoil. ARC Conf. Proc. 220.

²³Markovin M. V., Reshotko E and Herbert T., Transition in open flow systems-a reassessment, Bull. Am. Phys. Soc. 1994, 39:1882

²⁴Zang, Y., Street, R., and Koseff, J., "A dynamic mixed subgrid-scale model and its application to turbulent recirculating flows," Physics of Fluids, Vol. A5 (12), 1993, pp. 3186-3196.

²⁵Oi, M., McAuliffe, B., Han, E., Scholz, U., and Kahler, C., "Comparison of laminar separation bubbles measurements on low Reynolds number airfoil in three facilities," Proc. of the 35th Fluid Dynamics Conference and Exhibit, Toronto, Ontario, Canada, AIAA-2005-5149, 2005.